Acoustic tones generated by impinging jets: Differences between laminar and highly-disturbed nozzle-exit boundary layers

Mathieu Varé, Christophe Bogey

International Journal of Aeroacoustics
0(0):2–23

DOI: 10.1177/ToBeAssigned
www.sagepub.com/
SAGE

Acoustic tones generated by impinging jets: differences between laminar and highly-disturbed nozzle-exit boundary layers

Mathieu Varé[1] and Christophe Bogey[1]

Abstract

The differences between the acoustic tones generated by impinging jets with laminar and highly-disturbed nozzle-exit boundary layers are investigated. For that, jets at Mach numbers between 0.6 and 1.3 impinging on a flat plate at a distance of 8 nozzle radii from the nozzle exit are computed using large-eddy simulations. The amplitudes of the tones generated by the jets through feedback loops establishing between the nozzle and the plate are found to be significantly affected by the exit turbulent disturbances. In the present study, overall, they are lower for the initially laminar jets than for the initially disturbed ones. The level decrease varies from a few dB up to 15 dB, depending on the tones, which can change the frequencies of the dominant tones and the numbers and azimuthal structures of their associated feedback modes. For Mach numbers 0.75 and 0.8, for instance, the dominant tone frequencies are approximately two times lower for the initially laminar jets than for the other ones, yielding a better agreement with experiments of the literature in the former case. For a Mach number of 1.1, as a second example, the dominant tone is associated with the axisymmetric third feedback mode in the laminar case but with the helical fifth feedback mode in the disturbed case. The differences in the tone amplitude are finally discussed by estimating the power gains of the shear-layer instability waves between the nozzle and the plate using linear stability analysis for the axisymmetric mode. In most cases, at the frequency of a specific tone, the higher the gain, the stronger the acoustic tone.

Keywords
jet noise, impinging jet, tones, nozzle-exit conditions, LES

1 Introduction

Intense acoustic tones are known to be produced by high-speed jets impinging on a flat plate. They have been first noticed for high subsonic jets in many experimental works, such as those of Marsh[1], Preisser[2], Neuwerth[3] or Ho & Nosseir[4,5]. They were later found to be emitted by supersonic jets, as shown in the experiments of Norum[6], Krothapalli *et al.* [7] and Henderson *et al.* [8–10] and in the simulations of Dauptain *et al.* [11] and Gojon *et al.* [12–14], for example. Similar tones are also observed for jets impinging on edges[15] and perforated or inclined plates[16–19]. The tone frequencies exhibit a staging behaviour with the nozzle-to-plate distance, which has led Powell[15] to attribute their generation to aeroacoustic feedback loops establishing between the nozzle and the plate. The downstream component of the loops consists of the flow disturbances convected in the jet mixing layers, related to Kelvin-Helmholtz instability waves. The upstream component is formed by upstream-propagating guided jet waves[20], defined by specific dispersion relations and organized into azimuthal and radial modes. The latter waves also play a role in other resonance phenomena, such as in jet-flap interactions[21,22] and screech noise generation[23–26]. They are also responsible for the production of acoustic tones in the near pressure fields of free jets[27–30].

The properties of the feedback mechanisms in impinging jets are affected by the jet Mach number. Ho & Nosseir[4,5] observed experimentally that no feedback loop establishes for Mach numbers lower than 0.7. In other experiments[3,20,31], only an axisymmetric feedback mode is found for subsonic jets whereas both axisymmetric and helical feedback modes can be noticed for supersonic jets. The influence of the Mach number on the feedback frequencies has also been investigated experimentally by Jaunet *et al.* [32] and numerically by Varé & Bogey[33] for jets at Mach numbers varying between 0.6 and 1.3. The variations of the tone Strouhal numbers $St = fD/u_j$ with the Mach number in these two studies, where f is the frequency, D the nozzle-exit diameter and u_j the jet velocity, are shown in figure 1 for the Mach numbers considered in this work. In both cases, a staging behaviour of the tone frequencies with the Mach number is remarked. The tone frequencies are located in the allowable frequency bands of the free-stream upstream-propagating guided jet waves, as expected given that these waves close the feedback loop. However, except for Mach numbers 1 and 1.1, they are significantly higher in the simulations than in the experiments. This discrepancy was

[1] Univ Lyon, École Centrale de Lyon, INSA Lyon, Université Claude Bernard Lyon I, CNRS
Laboratoire de Mécanique des Fluides et d'Acoustique, UMR 5509
F-69134 Ecully, France

Corresponding author:
Mathieu Varé
Email: mathieu.vare@ec-lyon.fr

assumed to be due to differences in the nozzle-exit conditions which correspond to highly-disturbed ones in the simulations and were unknown in the experiments. Among the nozzle-exit conditions, the state of the boundary layers at the nozzle exit may be of great importance. Indeed, for free jets, the laminar or turbulent state of the nozzle-exit boundary layers strongly affects the flow development and the noise generation mechanisms, as documented in many papers [34–37]. For initially laminar jets, roll-ups of the shear layer and pairings of vortical structures occur, which is not the case for initially turbulent jets. Strong pressure waves are radiated by these vortex pairings, leading to higher noise levels compared with those for initially turbulent jets.

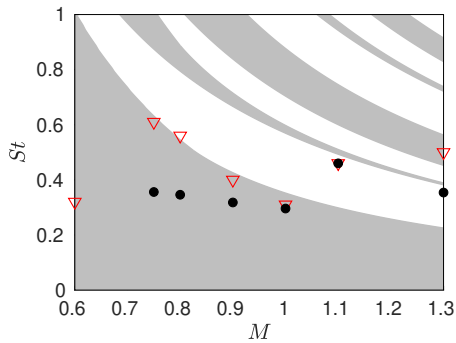

Figure 1. Variations of the frequencies of the near-nozzle tones generated by jets impinging on a plate at a distance of 8 nozzle radii from the nozzle with the Mach number: ▽ dominant tones in the LES of Varé & Bogey [33] for initially highly-disturbed jets, • measurements of Jaunet *et al.* [32], (grey shading) allowable frequency bands of the free-stream upstream-propagating guided jet waves.

For impinging jets, despite the preceding studies, the influence of the initial state of the boundary layer on resonance mechanisms is unfortunately still unclear. Therefore, the effects of this state on the establishment of feedback loops between the nozzle and the plate and on the variations of the tone properties with the Mach number, namely their frequencies, amplitudes and azimuthal structures, need to be highlighted.

In the present work, the differences between the acoustic tones created by impinging jets with laminar and highly-disturbed nozzle-exit conditions are investigated. For that, fourteen impinging jets at Mach numbers varying between 0.6 and 1.3 are simulated using large-eddy simulations (LES). The supersonic ones are nearly perfectly expanded. The jets are at a Reynolds number of 10^5 and they impinge on a plate located at the same nozzle-to-plate distance L as in the experiments of Jaunet *et al.* [32], namely 8 nozzle radii r_0. Half of the jets have initially laminar boundary layers and the other half have highly-disturbed nozzle-exit boundary layers with a peak turbulent intensity of 9%. The first objective of this work is to compare the characteristics of the acoustic tones produced by impinging jets for the two nozzle-exit conditions. For that purpose, the flow and sound fields are described. The near-nozzle pressure spectra are examined

to highlight the emergence of tones. The contributions of the first two azimuthal modes to the pressure fields are investigated to determine the azimuthal structure of the jets at the tone frequencies. The variations of the frequencies, amplitudes, widths and prominence of the tones with the Mach number are detailed. Another aim of the work is to study the influence of the initial flow conditions on the flow development of the jets by examining velocity spectra in the shear layer. The last objective of this paper is to explain the variations of the tones characteristics with the initial state of the jet mixing layer. To this end, the power gains of the Kelvin-Helmholtz instability waves between the nozzle and the plate are computed at the tone frequencies.

This paper is organized as follows. The jet parameters and the numerical methods used in the LES are documented in section 2. The results of the simulations are presented in section 3. Vorticity and pressure snapshots, mean and turbulent flow fields and pressure spectra are first described. The variations of the frequencies, amplitudes, widths and prominences of the tones with the Mach number are shown for both initially laminar and highly-disturbed jets. The velocity spectra in the shear layer are presented. The amplification rates of the shear-layer instability waves between the nozzle and the plate are evaluated at the tone frequencies using linear stability analysis. Finally, concluding remarks are given in section 4.

2 Parameters

2.1 Jet parameters

The parameters of the jets computed in this work are gathered in table 1. The jets have a Reynolds number $Re_D = u_j D/\nu$ of 10^5, where u_j is the jet velocity, D the nozzle diameter and ν the air kinematic viscosity. They originate at $z = 0$ from a cylindrical nozzle of radius r_0 and length $2r_0$, and are at ambient pressure and temperature $p_0 = 10^5$ Pa and $T_0 = 293$ K. They impinge on a plate located at $L = 8r_0$ downstream of the nozzle exit, as in the experiments of Jaunet *et al.* [32] At the nozzle inlet, a Blasius laminar boundary-layer profile with a thickness of $0.15r_0$ is imposed for the velocity, as done in previous simulations of free jets with tripped boundary layers[29]. In the pipe, the boundary layers are tripped or not, yielding highly-disturbed or fully laminar nozzle-exit boundary layers. Seven jets are tripped by adding vortical disturbances uncorrelated in the azimuthal direction in the boundary layer at $z = -r_0$ to create velocity fluctuations at the nozzle exit, using a procedure described in Bogey *et al.* [38] They have been investigated in Varé & Bogey[33]. The seven other jets are untripped. For both exit boundary-layer states, the jets have Mach numbers of $M = 0.6$, 0.75, 0.8, 0.9, 1, 1.1 and 1.3. The supersonic jets are nearly ideally expanded. For all jets, the nozzle-exit mean velocity profiles look like each other. They are similar to the nozzle-inlet boundary-layer profile of momentum thickness $\delta_\theta = 0.018r_0$, close to that in the experiments of Zaman[34]. They are represented in Varé & Bogey[33].

The profiles of root-mean-square (r.m.s.) axial velocity fluctuations at the nozzle exit are presented in figure 2. In all cases, the turbulent intensity reaches a peak value near the nozzle wall. For the untripped jets in figure 2(a), the peak value increases with the

jet tripping	Re_D	M	$\delta_\theta(z=0)/r_0$	$\max\langle u_z'^2\rangle/u_j$
yes	10^5	0.6-1.3	0.018	9%
no	10^5	0.6-1.3	0.018	$\leq 2\%$

Table 1. Parameters of the jets: jet tripping, Reynolds number Re_D, Mach number M, boundary-layer momentum thickness $\delta_\theta(z=0)$ and maximum turbulent intensity $\max\langle u_z'^2\rangle/u_j$ at the nozzle exit.

Mach number, from 0.25% at $M=0.6$ up to 1.45% at $M=1.3$, while for the tripped jets in figure 2(b), it is equal to 9 % for all Mach numbers, as intended. The nozzle-exit velocity fluctuations for the untripped jets are not zero as their mixing layers are excited by upstream-propagating pressure waves.

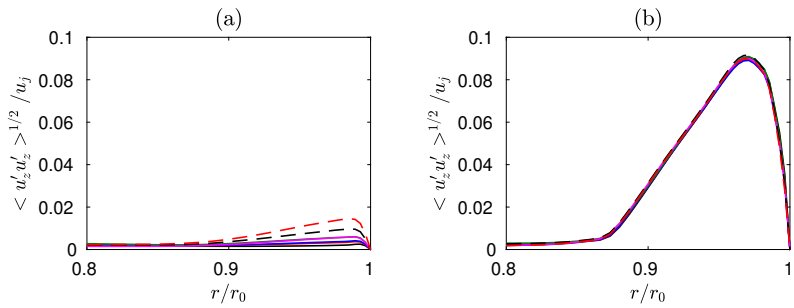

Figure 2. Nozzle-exit profiles of r.m.s. values of axial velocity for the jets with (a) untripped and (b) tripped boundary layers at — $M=0.6$, — $M=0.75$, — $M=0.8$, — $M=0.9$, — $M=1$, - - - $M=1.1$ and - - - $M=1.3$.

2.2 Numerical parameters

The numerical methods used are similar to those in recent LES of subsonic [18,33] and supersonic [39,40] impinging jets. In the simulations, the unsteady compressible Favre-filtered Navier-Stokes equations, namely the equations of conservation of mass, momentum and energy, are solved in cylindrical coordinates (r,θ,z) using an OpenMP based in-house solver. A second-order, six-stage Runge-Kutta algorithm [41] is employed for time-integration and the spatial derivatives are computed with eleven-point low-dispersion finite-difference schemes [42]. At the end of each time step, a selective filtering is applied to remove grid-to-grid oscillations [41]. This filter also acts as a subgrid-scale model by relaxing turbulent energy near the grid cut-off frequency, without affecting the scales discretized by more than five points per wavelength [43]. No-slip and adiabatic wall conditions are imposed to the plate and nozzle walls. In order to handle possible shocks created by the jet impingement in the jet potential core, a damping procedure using a dilatation-based shock detector and a second-order filter is used to remove

Gibbs oscillations in the vicinity of shocks for $z \geq 3r_0$ [44]. The radiation boundary conditions of Tam & Dong [45] are implemented at the radial and lateral boundaries of the computational domain. They are associated with sponge zones combining grid stretching and Laplacian filtering to prevent significant spurious reflections [46]. The method of Mohseni & Colonius [47] is applied to treat the singularity on the jet axis. The closest point to the axis is located at $r = \Delta r/2$, where Δr is the radial mesh size near the jet axis. The azimuthal derivatives near the jet axis are evaluated with fewer points than permitted by the grid to increase the time step of the simulations [48]. More precisely, the effective azimuthal resolution near the origin of the polar coordinates is reduced down to $2\pi/16$. The time step is set to satisfy the Courant-Friedrichs-Lewy stability criterion with acoustic Courant numbers of 1.1, 0.9, 0.8 and 0.7 for $M = 0.6$, 0.75, 0.8 and $M \geq 0.9$, respectively.

2.3 Computational parameters

The same radial and axial mesh grids are used for all simulations. They are detailed in Varé & Bogey [33]. The numbers of points in the radial and axial directions are equal to 559 and 1124. In the azimuthal direction, there are 1024 points for the tripped jets and 256 points for the untripped jets, which yields a total number of 640 and 160 million points, respectively. The grid extends out to $r = 15r_0$ in the radial direction and down to $z = 8r_0$ in the axial direction. The radial mesh spacing is equal to $\Delta r = 0.014r_0$ on the jet axis and decreases down to $\Delta r = 0.0036r_0$ at $r = r_0$ in the shear layer. It then increases up to a value of $\Delta r = 0.075r_0$ for $r > 6.2r_0$, which yields Strouhal numbers St varying from 4.1 for $M = 1.3$ up to 8.9 for $M = 0.6$ for an acoustic wave with five points per wavelength. The axial mesh spacing Δz is minimum and equal to $\Delta z = 0.0072r_0$ at the nozzle exit, and maximum and equal to $\Delta z = 0.012r_0$ between $z = 2r_0$ and $z = 6r_0$. Farther downstream, the axial mesh spacing decreases down to $\Delta z = 0.0072r_0$ on the plate at $z = 8r_0$. The extremum values of the mesh spacings and the stretching rates are the same as in the study of Bogey [49], where a grid convergency study was performed for a free jet with the same ejection conditions as the present impinging tripped jet at $M = 0.9$.

The variations of the mesh spacings in the wall-normal direction Δr^+ and Δz^+ obtained on the nozzle inner wall and on the plate in wall units, respectively, are presented in figure 3 for the untripped jets. The results for the tripped jets are not shown as they look like those for the untripped jets. In the nozzle in figure 3(a), for all jets, the mesh spacing Δr^+ does not vary much with the axial distance. It decreases with the Mach number, from 3 at $M = 0.6$ down to 2 at $M = 1.3$. These values are higher than 1, indicating that the near-wall turbulence is not fully resolved, but they are sufficiently small for turbulent structures to develop inside the nozzle [56]. On the plate in figure 3(b), for all jets, the axial mesh spacing Δz^+ reaches a maximum value near $r = 2r_0$. This value is equal to 12 for $M = 0.6$ and decreases with the Mach number, down to 10.8 for $M = 1.3$. Farther from the center of the plate, the mesh spacing Δz^+ decreases in all cases. It remains much higher than 1, showing that the wall jet is not well resolved [51–54]. However, the noise

radiated by the wall jet can be expected to be weaker than the noise created by the jet flow structures, due to the low wall jet velocity compared with the jet exhaust velocity.

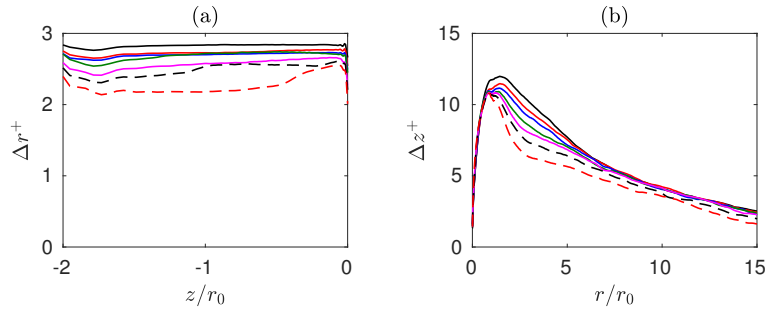

Figure 3. Variations of (a) the radial mesh spacing Δr^+ on the nozzle wall and (b) the axial mesh spacing on the plate, in wall units, for the untripped jets at —— $M = 0.6$, —— $M = 0.75$, —— $M = 0.8$, —— $M = 0.9$, —— $M = 1$, - - - $M = 1.1$ and - - - $M = 1.3$.

The results presented in this paper are obtained after simulation times of $500r_0/u_j$ for the tripped jet at $M = 1.3$ and $1,000r_0/u_j$ otherwise. During the simulations, density, velocities and pressure along the jet centerline at $r = 0$, along the nozzle-lip line at $r = r_0$, on the surfaces at $r = 15r_0$, $z = -2r_0$, $z = 0$ and on the plate at $z = L$ are recorded at a sampling frequency enabling spectra to be computed up to $St = 12$. Density, velocity components and pressure are saved for the azimuthal angles $\theta = 0$, 90, 180 and 270 degrees at a halved frequency. The azimuthal Fourier coefficients of the density, pressure and velocity fields are also computed up to the mode $n_\theta = 4$ for $0 \leq r \leq 15r_0$ and $0 \leq z \leq 8r_0$. The spectra are estimated from these recordings and they are averaged in the azimuthal direction when possible.

3 Results

3.1 Snapshots of the flow and acoustic fields

Snapshots of the vorticity norm and of the pressure fluctuations obtained for the jets at Mach numbers of 0.6, 0.8, 1.1 and 1.3 with untripped and tripped boundary layers are presented in figure 4 on top and bottom, respectively. For brevity, the results for the jets at $M = 0.75$, 0.9 and 1 are not shown because they resemble those for $M = 0.8$ in the former case and for $M = 1.3$ for the latter cases. In the vorticity fields, for the untripped jets, in figure 4(a-d), roll-ups of the shear layer and pairings of large coherent structures are observed from the nozzle exit down to $z = 4r_0$ whereas for the tripped jets in figure 4(e-h), fine-scale turbulent structures are found near the nozzle exit, indicating highly-disturbed mixing layers. In all cases, the shear layers spread with the axial distance and they impinge on the plate, which creates a wall jet.

In the pressure fields, for the tripped jets for $M \geq 0.8$ in figure 4(f,g,h), strong low-frequency pressure waves originating from the jet impingement area on the plate

dominate in the sound field. Their wavefronts are periodically spaced, indicating a tonal radiation. They also propagate in the upstream direction inside the jet column. For the untripped jets at $M = 1.1$ and 1.3 in figures 4(c,d), pressure waves similar to those for the corresponding tripped jets are observed. However, their amplitudes are lower than for the tripped jets, suggesting a weaker resonance. For the untripped jets at $M = 0.6$ and 0.8 and the tripped jet at $M = 0.6$ in figures 4(a,b,e), high-frequency pressure waves are seen to be produced near the plate and the wall jet and to propagate in the upstream direction. The sound radiation does not appear to be tonal in the three cases.

3.2 Mean flow fields

The centerline mean axial velocity, the shear-layer momentum thickness and the nozzle lip-line axial turbulent intensity obtained between the nozzle exit and the plate are shown in figure 5. In figure 5(a,d), for all jets, the centerline mean velocity remains close to the exit velocity down to $z = 6.5r_0$ and falls down to zero on the plate. For the supersonic jets, small oscillations are noticed at the nozzle exit, due to the presence of weak shock cells. For $M \geq 1.1$ for the initially laminar jets and for $M \geq 0.9$ for the initially disturbed jets, oscillations of higher amplitude are also observed for $z \geq 4r_0$, suggesting that they are related to compression cells created by the jet impingement on the plate.

In figures 5(b,e), for given exit boundary-layer conditions, the shear-layer thicknesses are similar for all Mach numbers. However, they are significantly different in the tripped and the untripped cases. The mixing layer starts to spread at $z = 2r_0$ for the untripped jets in figure 5(b) and at $z = 0$ for the tripped jets in figure 5(e). Then, the shear-layer thickness grows almost linearly down to $z \approx 6.5r_0$. The shear-layer growth rates are lower for the tripped jets than for the untripped ones, which is consistent with the results obtained for free jets[36]. Near the plate, in all cases, the shear-layer thickness increases due to the formation of a wall jet.

Regarding the turbulent intensities, for the untripped jets they are very low down to $z = r_0$ and then quickly increase up to about 20% at $z = 3r_0$ in figure 5(c). This increase is related to the vortex pairings occurring in the shear layer. Farther downstream, the levels do not vary much down to $z = 7r_0$ and finally fall to zero on the plate. For the tripped jets, the axial turbulent intensities sharply rise between the nozzle exit and $z = 2r_0$ in figure 5(f). Then, they do not vary much down to $z = 7r_0$, taking values between 13% for $M = 0.9$ and 16% for $M = 0.6$, and finally collapse to zero on the plate. The peak values of the axial turbulent intensity along the nozzle-lip line are significantly lower for the tripped jets than for the untripped ones, as in free jets.

3.3 Near-nozzle pressure spectra

The pressure spectra obtained at $z = 0$ and $r = 1.5r_0$ near the nozzle are displayed in figure 6 for the jets at $M = 0.6$, 0.8, 1.1 and 1.3 as a function of the Strouhal number. The spectra for the jets at $M = 0.75$, 0.9 and 1 are not shown because they show the same trends as those for $M = 0.8$ in the first case and those for $M = 1.3$ in the two last cases. For all Mach numbers, the broadband levels are approximately 5 dB higher for the untripped jets than for the tripped ones. For $M = 0.6$, in figure 6(a), no tones are clearly

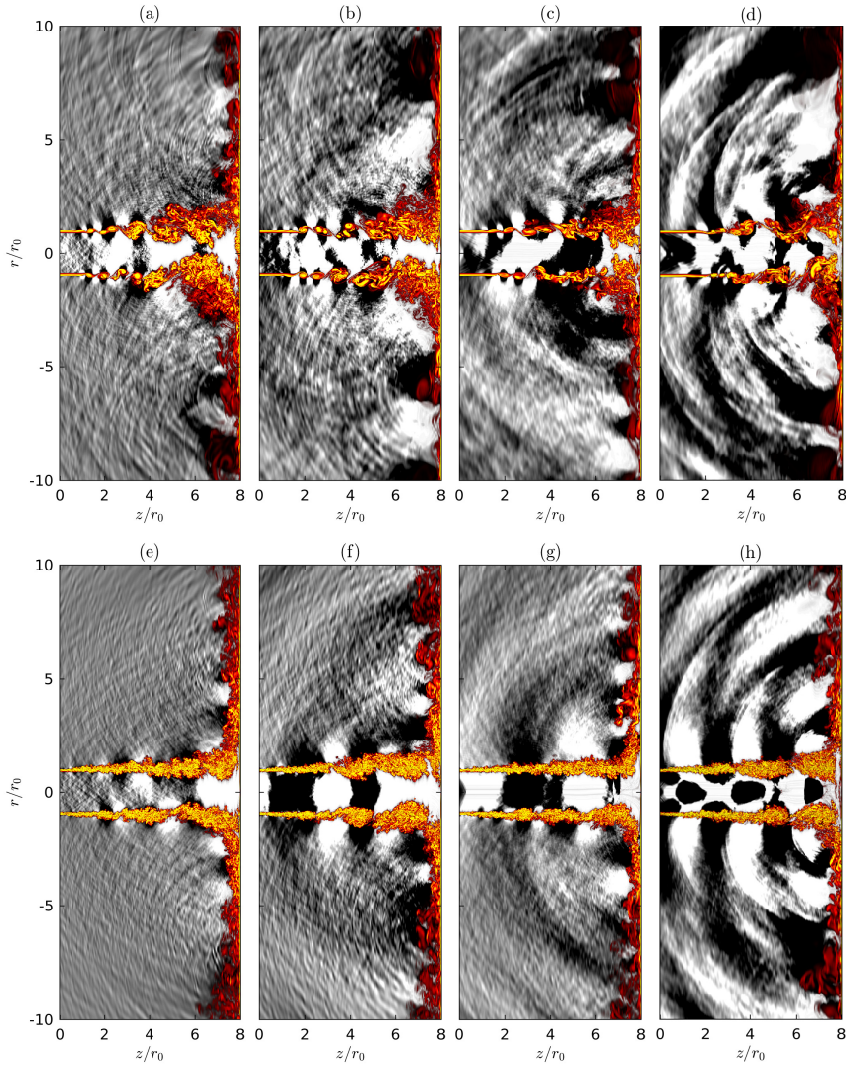

Figure 4. Snapshots in the (z, r) plane of vorticity norm in the flow and of pressure fluctuations outside for the (top) untripped and (bottom) tripped jets at (a,e) $M = 0.6$, (b,f) $M = 0.8$, (c,g) $M = 1.1$ and (d,h) $M = 1.3$. The color scales range from 0 to $15u_j/r_0$ for vorticity, from black to yellow, and between (a,b,e,f) $\pm 0.005p_0$ and (c,d,g,h) $\pm 0.01p_0$ for pressure, from black to white.

seen in the spectra, indicating the absence of marked resonance phenomena. For $M = 0.8$ in figure 6(b), a tone appears 15 dB higher than the broadband levels at $St = 0.51$ for

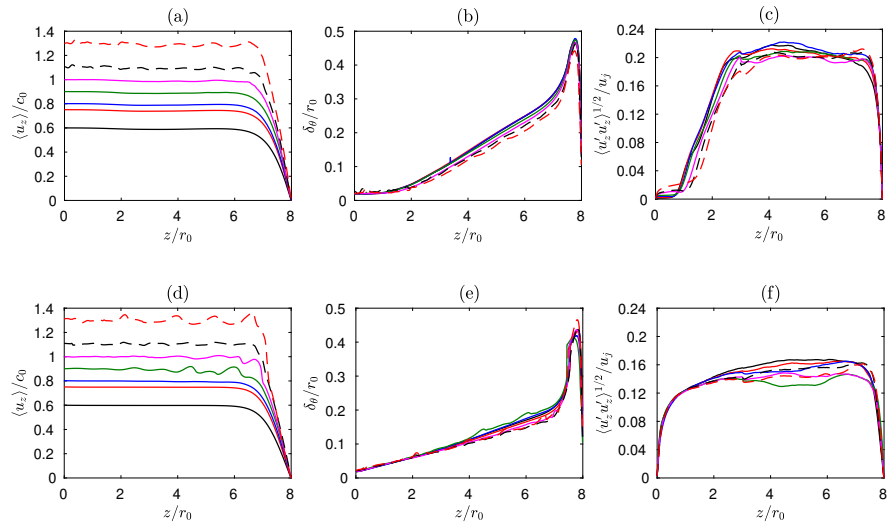

Figure 5. Variations of (a,d) the centerline mean axial velocity $\langle u_z\rangle/c_0$, (b,e) the shear-layer momentum thickness δ_θ/r_0 and (c,f) the axial turbulent intensity $\langle u'_z u'_z\rangle^{1/2}/u_j$ at $r = r_0$ for the (top) untripped jets and (bottom) tripped jets; — $M = 0.6$, — $M = 0.75$, — $M = 0.8$, — $M = 0.9$, — $M = 1$, - - - $M = 1.1$ and - - - $M = 1.3$.

the tripped jet but not for the untripped one. In the latter case, the peak level is located at a lower Strouhal number of $St = 0.37$. For higher Mach numbers in figures 6(c,d), peaks emerging by more than 10 dB are found for both tripped and untripped jets. Their frequencies are similar in the two cases. They are equal to $St = 0.29$, 0.46 and 0.66 for $M = 1.1$ in figure 6(c) and to $St = 0.35$ and 0.51 for $M = 1.3$ in figure 6(d). For $M = 1.1$, the dominant peak changes with the nozzle-exit condition. Indeed, it is located at $St = 0.29$ for the untripped jet and at $St = 0.46$ for the tripped one. Regarding the tone amplitudes, in most cases, they are higher for the initially highly-disturbed jets than for the initially laminar jets.

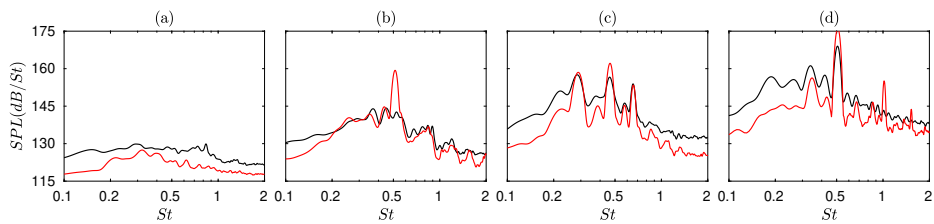

Figure 6. Sound pressure levels (SPL) at $z = 0$ and $r = 1.5r_0$ for (a) $M = 0.6$, (b) $M = 0.8$, (c) $M = 1.1$ and (d) $M = 1.3$; — untripped and — tripped jets.

The variations of the frequencies of the dominant peaks with the Mach number are plotted in figure 7, alongside with those in the experiments of Jaunet *et al.* [32] For $M = 0.9$, 1 and 1.3, the frequencies of the dominant peak are very similar for the untripped and tripped jets. For the other Mach numbers, however, they differ. The peak level frequencies for the untripped cases are higher for $M = 0.6$ and lower for $M = 0.75$, 0.8 and 1.1 than in the tripped cases. Regarding the tone frequencies in the experiments of Jaunet *et al.* [32], they are similar to those for the untripped jets for $M = 0.75$ and 0.8, to those for the tripped jet for $M = 1.1$ and to those for both jets for $M = 1$. These results suggest that the discrepancies observed between the LES and the experiments are due to differences in the nozzle-exit conditions.

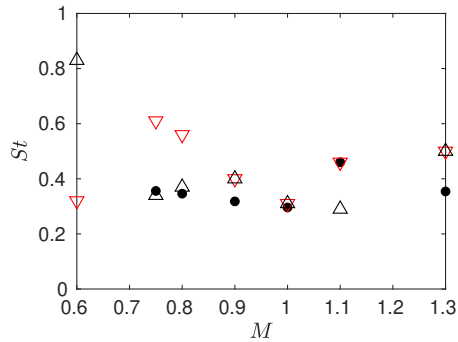

Figure 7. Variations of the near-nozzle peak Strouhal numbers with the Mach number: dominant peaks in the LES for the △ untripped and ▽ tripped jets ; • measurements of Jaunet *et al.* [32] for $L = 8r_0$.

The tones are produced by feedback loops establishing between the nozzle and the plate. To predict the feedback frequencies, the feedback period is usually approximated as the sum of two characteristic times[4], namely the time of convection of the flow structures from the nozzle exit down to the plate and the time of propagation of the acoustic waves travelling upstream at the ambient speed of sound, yielding

$$f = \frac{N\langle u_c \rangle}{L(1 + M_c)} \tag{1}$$

where $\langle u_c \rangle$ is the mean convection velocity between the nozzle and the plate, $M_c = \langle u_c \rangle / c_0$ is the convection Mach number and N is an integer representing the order of the feedback mode. The integer N corresponds to the number of coherent structures between the nozzle and the plate. Each tone frequency can thus be related to an integer N, given in what follows.

3.4 Azimuthal decomposition of the pressure spectra

The contributions of the first two azimuthal modes to the spectra at $z = 0$ and $r = 1.5r_0$ are presented in figure 8 for $M = 0.6$, 0.8, 1.1 and 1.3, as previously. The dominant

tone is found for the helical mode $n_\theta = 1$ for the tripped jet at $M = 1.1$, and for the axisymmetric mode in all other cases. For $M = 0.6$ in figures 8(a,e), the Strouhal number of the dominant peak differs with the nozzle-exit conditions. It is equal to 0.83 for the untripped jet and to 0.32 for the tripped one. For $M = 0.8$ in figures 8(b,f), peaks are found for $n_\theta = 0$ at the same Strouhal numbers $St = 0.37$, 0.45, 0.51 and 1.2 for the tripped and untripped jets. The dominant peak frequency however differs. For the untripped jet, the peak at $St = 0.37$ is slightly higher than the other peaks, whereas for the tripped jet, the dominant peak emerges strongly by 20 dB from the broadband levels at $St = 0.51$. For $n_\theta = 1$, a peak is observed at $St = 0.8$ for the two jets. For $M = 1.1$ in figures 8(c,g), the contributions of the two azimuthal modes to the spectra are similar for the two initial flow conditions. The tones at $St = 0.29$ and 0.66 are linked to the mode $n_\theta = 0$ and the tone at $St = 0.46$ is related to the mode $n_\theta = 1$. They are more intense for the tripped jet than for the untripped one. Moreover, the dominant tone is found at $St = 0.29$ for the untripped jet but at $St = 0.46$ for the tripped jet, for $n_\theta = 0$ and $n_\theta = 1$, respectively. In this case, the dominant jet oscillation mode changes with the nozzle-exit conditions. Finally, for $M = 1.3$ in figures 8(d,h), in both cases, the dominant peak at $St = 0.51$ is associated with the mode $n_\theta = 0$ and secondary peaks are noticed at $St = 0.2$ for $n_\theta = 0$ and around $St = 0.35$ for $n_\theta = 1$. The peaks are stronger by 5 to 15 dB for the initially highly-disturbed jet than for the other jet.

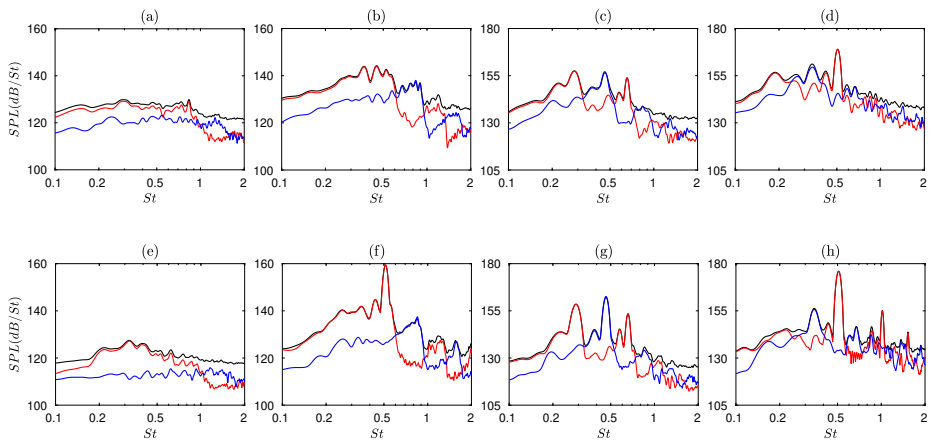

Figure 8. Sound pressure levels (SPL) at $z = 0$ and $r = 1.5r_0$ for (top) untripped and (bottom) tripped jets at (a,e) $M = 0.6$, (b,f) $M = 0.8$, (c,g) $M = 1.1$ and (d,h) $M = 1.3$; — full signal, — $n_\theta = 0$ and — $n_\theta = 1$.

The peak Strouhal numbers in the near-nozzle spectra for the first two azimuthal modes are plotted in figure 9 as a function of the Mach number. For $n_\theta = 0$, in figure 9(a), the peak frequency is about three times higher in the untripped case than in the tripped case for $M = 0.6$. For $M = 0.75$ and 0.8, on the contrary, the peak frequencies are significantly lower in the first case. For higher Mach numbers, they are similar for the

two initial flow conditions. For $n_\theta = 1$ in figure 9(b), the peak frequencies are also the same for the tripped and untripped jets at all Mach numbers.

The frequency ranges of the free-stream upstream-propagating guided jet waves with a non-negligible amplitude on the nozzle lip line estimated using a vortex-sheet model[29,30] are indicated. Each band is associated with a radial mode of the guided jet waves, whose order n_r increases with the frequency. For $n_\theta = 0$, the dominant tones lie in the band of the first radial mode for $M \leq 1.1$ and of the second radial mode for $M = 1.3$. For $n_\theta = 1$, they are all located in the band of the first radial mode. In particular, for $n_\theta = 0$ and $n_r = 1$ in figure 9(a), the dominant tones are close to the mode cutoff frequency for the jets emitting intense tones, namely for all jets at $M \geq 0.9$ and for the tripped jets at $M = 0.75$ and 0.8, as observed for the near-nozzle tones of free jets[29]. In contrast, they are far from the band upper limit for the untripped jets at $M = 0.75$ and 0.8 and the tripped jet at $M = 0.6$ generating no tones. For the untripped jet at $M = 0.6$, however, the peak frequency is near the band limit, suggesting that the small peak at $St = 0.83$ in the pressure spectrum is produced by a weak resonance.

In figure 9, the frequencies predicted by equation (1) for different N are also plotted. For both azimuthal modes, the peak frequencies fall close to the frequencies curves thus obtained. For $n_\theta = 0$ for the tripped jets, the mode order is equal to $N = 3$ for $M = 0.6$, jumps to $N = 6$ for $M = 0.75$, then as the Mach number increases, it decreases down to $N = 3$ at $M = 1.1$ and finally it is equal to $N = 6$ for $M = 1.3$. These changes in the feedback mode order is explained by the closure of the loops by the guided jet waves[33]. Indeed, the values of N vary so that the tone frequencies stay in the bands of the guided jet waves. Notably, for $n_\theta = 0$, the feedback mode N rises from $N = 3$ at $M = 1.1$ to $N = 6$ at $M = 1.3$ as the tonal frequency switches from the first radial mode of the guided jet waves to the second radial mode.

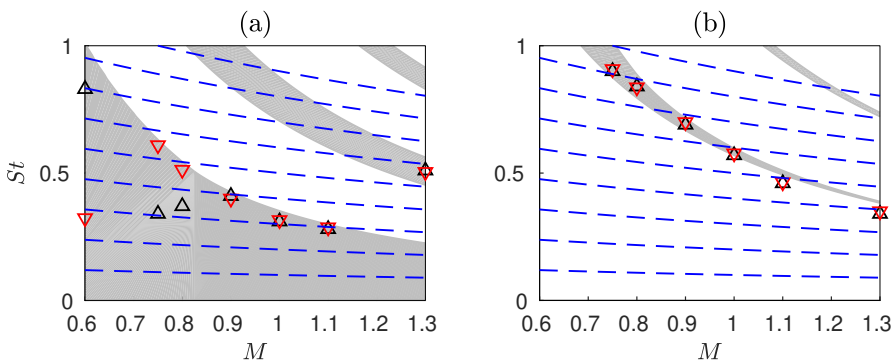

Figure 9. Variations of the peak Strouhal numbers in the near-nozzle pressure spectra with the Mach number for (a) $n_\theta = 0$ and (b) $n_\theta = 1$: △ untripped and ▽ tripped jets, (grey shading) allowable frequency bands of the free-stream upstream-propagating guided jet waves; - - - equation (1) with N varying from 1 to 9 and $\langle u_c \rangle = (2/3)u_j$.

To quantify the changes in the peak properties with the nozzle-exit conditions, the variations of the amplitude, width at half maximum and prominence of the near-nozzle tones with the Mach number for $n_\theta = 0$ are displayed in figure 10. The prominence is estimated as the difference between the peak level and the first minimum value reached for higher frequencies[29]. In figure 10(a), the peak levels are similar for the untripped and tripped jets for $M = 0.6$ and $M = 1.1$. For the other jet velocities, they are higher by 7 to 15 dB for the tripped jets. In figure 10(b), the peak widths are slightly larger for the tripped jets than for the untripped jets for $M \leq 0.8$ and $M = 1.3$. On the contrary, for the other Mach numbers, the peaks are two to three times thinner for the tripped jets. In figure 10(c), for $M = 0.6$, the peak at $St = 0.83$ in the spectrum for the untripped jet is found to emerge more strongly than the hump at $St = 0.33$ in the spectrum of the tripped jet. For higher Mach numbers, the peaks are more prominent for the highly-disturbed jets than for the initially laminar jets, which is most likely due to higher broadband levels in the latter case.

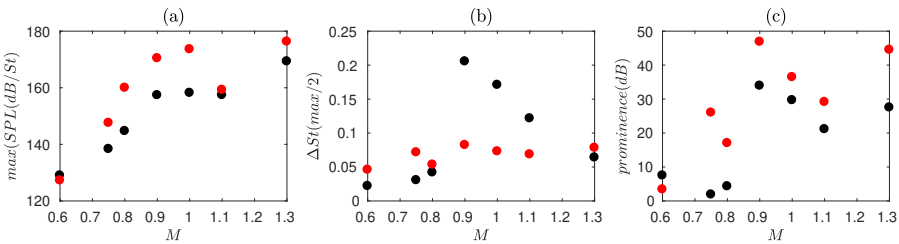

Figure 10. Variations of (a) the amplitude, (b) the width and (c) the prominence of the dominant near-nozzle tones with the Mach number for $n_\theta = 0$: ● untripped jets, ● tripped jets.

3.5 Shear-layer velocity spectra

To compare the development of the jet flow structures for the two different nozzle-exit conditions, the spectra of the radial velocity fluctuations in the shear layer at $r = r_0$ between the nozzle exit and the plate are represented in figure 11 for $M = 0.6$, 0.8, 1.1 and 1.3. For the untripped jets at $M = 0.6$ and 0.8 in figures 11(a,b), two spots of strong levels are visible. The first spot is found near the nozzle around $z = 2r_0$ for Strouhal numbers between 1.5 and 2. These frequencies are close to that of $St_D = 1.77$, corresponding to the frequency $St_\theta = f\delta_\theta(z = 0)/u_j = 0.016$ predicted for the most amplified Kelvin–Helmholtz instability waves at the nozzle exit using linear stability analysis[55]. The second spot lies between $z = 2r_0$ and $4.5r_0$ and around the first subharmonic of the initial most unstable frequency. Therefore, it results from the pairings of vortical structures in the shear layer. For the highly-disturbed jets at the $M = 0.6$ and 0.8 in figures 11(e,f), the velocity spectra strongly differ from those for the initially laminar jets. Only one large spot is visible for $z \geq 4r_0$ and for $St \leq 1$, farther downstream and at frequencies lower than the high-energy spots for the untripped cases. This spot can be related to the formation of large coherent flow structures in the shear

layers. For $M = 0.8$ in figure 11(f), two stripes are also observed at $St = 0.51$ and its first harmonic, indicating the development of flow structures at the feedback frequencies.

For the supersonic jets, in figures 11(c,d,g,h), the highest levels are located along thin lines starting at $z \approx 2r_0$ and extending down to the plate. These lines are found at the Strouhal numbers of the dominant tones in the pressure spectra, highlighting an effective and persistent forcing of the shear-layer flow structures by the upstream-propagating guided jet waves. Some differences between the results for the two initial flow conditions can be pointed out. First, for $M = 1.1$, the frequencies of the strongest levels are equal to $St = 0.66$ for the untripped jet in figure 11(c) but to $St = 0.46$ for the tripped jet in figure 11(g). Second, for $M = 1.3$, a high intensity line is observed at the first harmonic of the dominant frequency $St = 0.51$ for the highly-disturbed jet in figure 11(h), which is not the case for the other jet in figure 11(d).

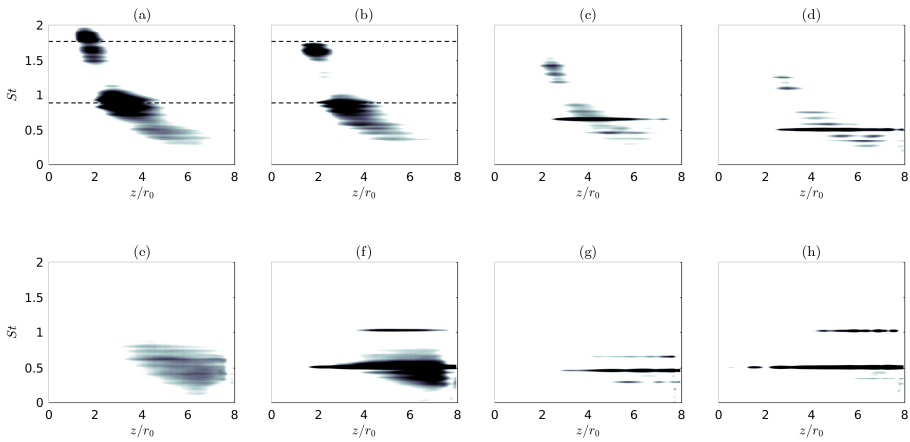

Figure 11. Power spectral densities of the fluctuations of radial velocity normalized by the jet velocity at $r = r_0$ between the nozzle and the plate for the (top) untripped and (bottom) tripped jets for (a,e) $M = 0.6$, (b,f) $M = 0.8$, (c,g) $M = 1.1$ and (d,h) $M = 1.3$, - - - $St_\theta = 0.016$ and 0.08. The color scale is 6 dB higher for the untripped jets than for the tripped ones and spreads over 3 dB, from white to black.

Spectra of the radial velocity fluctuations and the contributions of the first two modes to these spectra estimated near the nozzle and near the plate for $M = 0.6$, 0.8, 1.1 and 1.3 are presented. The spectra obtained near the nozzle at $r = r_0$ and $z = 0.4r_0$ are plotted in figure 12. For all jets, they are dominated by broad humps and narrow peaks. The humps are found near the most unstable frequencies calculated using linear stability analysis near the nozzle exit. They are visible for the full signals and for $n_\theta = 0$ and 1 for the untripped jets, but only for $n_\theta = 0$ and 1 for the other jets. The peaks are located at the same frequencies as those in the near-nozzle pressure spectra, highlighting a forcing of the flow by upstream-propagating guided jet waves[30]. They emerge more sharply for the

tripped jets, suggesting a stronger excitation of the flow by the upstream-propagating waves in this case.

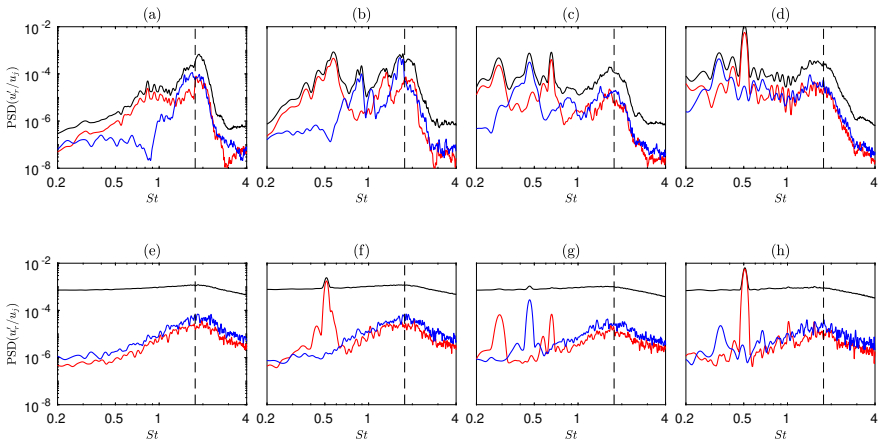

Figure 12. Power spectral densities of the fluctuations of radial velocity at $r = r_0$ and $z = 0.4r_0$ for the (top) untripped and (bottom) tripped jets for (a,e) $M = 0.6$, (b,f) $M = 0.8$, (c,g) $M = 1.1$ and (d,h) $M = 1.3$, —— full signal, —— $n_\theta = 0$ and —— $n_\theta = 1$, - - - $St_\theta = 0.016$.

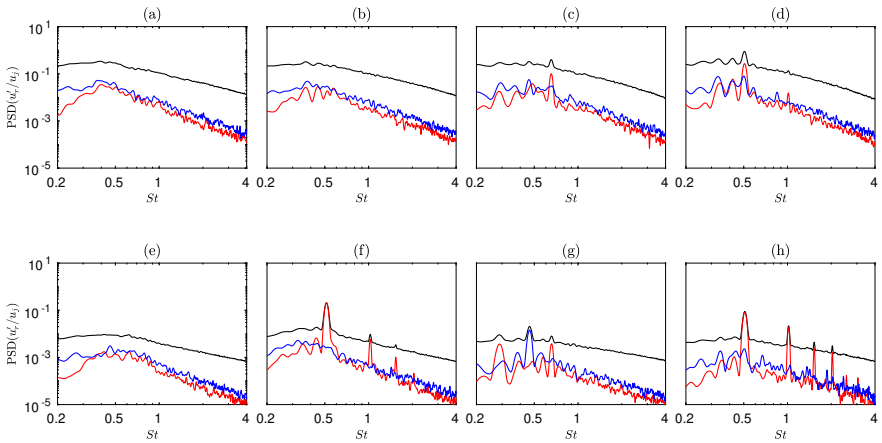

Figure 13. Power spectral densities of the fluctuations of radial velocity at $r = r_0$ and $z = 7r_0$ for the (top) untripped and (bottom) tripped jets for (a,e) $M = 0.6$, (b,f) $M = 0.8$, (c,g) $M = 1.1$ and (d,h) $M = 1.3$, —— full signal, —— $n_\theta = 0$ and —— $n_\theta = 1$.

The spectra of the velocity fluctuations obtained near the plate at $r = r_0$ and $z = 7r_0$ are presented in figure 13. Their levels are higher for the initially laminar jets than for the other ones, in agreement with the stronger shear-layer velocity fluctuations

in figures 5(c,f). They all display a low-frequency hump around $St = 0.5$ due to the presence of large-scale flow structures. Tones also appear in the spectra for the same Mach numbers, frequencies and azimuthal modes as in the near-nozzle velocity spectra, showing that flow structures develop at the feedback frequencies from the nozzle down to the plate. However, the tone emergence significantly differ for the two initial flow conditions. In particular, the tones are more prominent in the tripped jets than in the untripped ones, suggesting a stronger resonance for the first jets. For $M = 0.8$ and $M = 1.3$ in figures 13(b,f) and (d,h), the harmonics of the dominant tone for $n_\theta = 0$ can also be seen for the tripped jets but not for the untripped ones, supporting the latter claim.

3.6 Power gains of the Kelvin-Helmholtz instability waves between the nozzle and the plate

Finally, the total amplification rates of the instability waves between the nozzle and the plate are computed to discuss the origin of the differences of the amplitude of the near-nozzle tone with the state of the nozzle-exit boundary layer. For that, as done in a recent work[33], an inviscid spatial stability analysis is performed from the hyperbolic-tangent velocity profile[55]:

$$\frac{u_z(r)}{u_j} = \frac{1}{2}\left[1 - \tanh\left(\frac{1}{2}\frac{(r - r_0)}{\delta_\theta(z)}\right)\right] \tag{2}$$

where $\delta_\theta(z)$ is the shear-layer momentum thickness. The LES mean velocity profiles are not used directly because they contain strong flow oscillations near the plate, making the linear stability analysis difficult. As in previous investigations[56,57], the compressible Rayleigh equation is solved with a shooting technique[58], employing the Euler method for the integration step and the secant method for the search of the complex wavenumber. For a given Strouhal number St, the growth rates $-k_i$ of the instability waves, where k_i is the imaginary part of the wavenumber, are first evaluated at $z = 0$ for a hyperbolic-tangent profile of thickness $\delta_\theta(z = 0)$. The growth rates for the other axial locations are deduced from these results using a scaling with the shear-layer thickness[55]. Since the wavenumbers of the damped waves with $k_i \geq 0$ are not accurately estimated by the solving of the Rayleigh equation[58], their imaginary parts are set to zero.

The growth rates $-k_i r_0$ obtained for $n_\theta = 0$ between $z = 0$ and $8r_0$ are presented in figure 14 for the jets at $M = 0.6$, 0.8, 1.1 and 1.3. The spatial variations of the growth rates are similar for all jets. Near the nozzle, the rates are highest for Strouhal numbers higher than 1. Then the most unstable frequencies decrease with the axial distance due to the shear-layer thickening[57,59]. They are reduced down to $St = 0.5$ at $z = 2r_0$ and they reach Strouhal numbers lower than 0.2 near the plate. Therefore, at high frequencies, the instability waves grow over a very short distance to the nozzle exit whereas at low frequencies, they are amplified all over the nozzle-to-plate distance. For both untripped and tripped exit boundary layers, the growth rates decrease as the Mach number increases, because the jet flow is more stable for higher Mach numbers[55,58]. However, differences can be noticed between the two initial flow conditions. For instance,

downstream of the nozzle, the growth rates for $St \geq 0.5$ remain high over a longer distance for the untripped jets than for the tripped ones, typically of $2r_0$ in the first case and r_0 in the second. This can be due to the slower spreading of the mixing layer near the nozzle in the untripped jets, illustrated in figure 5(b,e). On the contrary, for $z \geq 4r_0$ and $St \leq 0.5$, the growth rates are lower for the untripped jets than for the tripped ones.

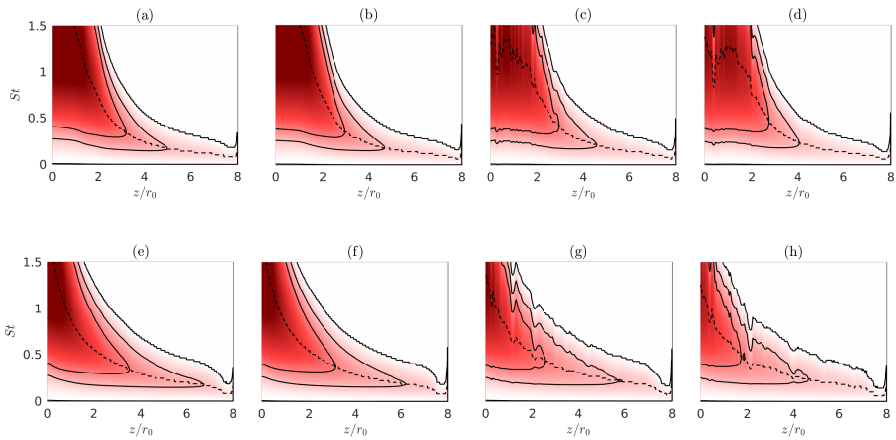

Figure 14. Instability growth rates $-k_i r_0$ for $n_\theta = 0$ as a function of the axial position z and of the Strouhal number St for the (top) untripped and (bottom) tripped jets and at (a,e) $M = 0.6$, (b,f) $M = 0.8$, (c,g) $M = 1.1$ and (d,h) $M = 1.3$, - - - most unstable frequencies. Contour lines for the levels 0, 0.5 and 1 are drawn in black. The colorscale ranges from 0 to 3, from white to red.

To quantify the amplification of the instability waves between the nozzle and the plate, the growth rates of the Kelvin-Helmholtz waves are integrated between $z = 0$ and L, as done in previous works[30,33,60–63], giving the power gain A:

$$A(St) = \exp\left(\int_0^{L=8r_0} -k_i(St, z)dz\right) \tag{3}$$

The power gains A_{untrip} and A_{trip} obtained for the untripped and tripped jets at the frequencies of the near-nozzle tones for $n_\theta = 0$ are provided in table 2. For each Mach number, the highest gain value is shown in bold. For $M = 0.6$, the gain is computed at the Strouhal number $St = 0.83$ at which there is a peak for the untripped jet but not for the tripped one. The value of the gain is higher in the first case than in the second case, which is consistent with the above. For Mach numbers between 0.75 and 1.1, the power gains at the tone frequencies are higher for the initially disturbed jets than for the other ones. The shear-layer instability waves at the feedback frequencies are thus more amplified between the nozzle and the plate in the first case, which can explain the stronger tones in

the near-nozzle pressure spectra. For $M = 1.3$, the highest power gain is obtained for the untripped jet. However, the near-nozzle acoustic tone is weaker for this jet than for the tripped jet. The reason for this mismatch is unclear. It can be due to uncertainties in the calculation of the gain, in particular the facts that a hyperbolic-tangent velocity profile is used and that the damping rates of the evanescent instability waves are not taken into account when $-k_i < 0$.

M	0.6	0.75	0.8	0.9	1	1.1	1.3
St	0.83	0.61	0.51	0.40	0.31	0.29	0.51
$A_{untrip}(St)$	**566**	180	117	55	39	37	**74**
$A_{trip}(St)$	212	**226**	**185**	**104**	**137**	**106**	37

Table 2. Peak Strouhal numbers St and power gains A_{untrip} and A_{trip} of the shear-layer instability waves between the nozzle and the plate for the untripped and tripped jets at these frequencies, for $n_\theta = 0$.

4 Conclusion

In this paper, the differences between the acoustic tones generated by impinging jets with laminar and highly-disturbed nozzle-exit conditions have been investigated using LES for Mach numbers varying between 0.6 and 1.3. These tones are produced by feedback mechanisms establishing between the nozzle and the plate. Their amplitudes are higher for the highly-disturbed jets than for the initially laminar ones. These variations in the tones amplitudes with the nozzle-exit conditions can change the dominant peak frequency and its azimuthal mode. For instance, for $M = 1.1$, the strongest tone is associated with an axisymmetric mode for the untripped jet and with the first helical mode for the tripped one. Moreover, for $M = 0.75$ and 0.8, the dominant peak frequency is about two times lower for the initially laminar jets than for the highly-disturbed ones, yielding frequencies closer to those in the experiments of Jaunet *et al.* [32] in the first case. The initial flow conditions can thus explain some of the discrepancies in the tonal frequencies between previous simulations and the experiments. However, these discrepancies remain for $M = 0.9$ and $M = 1.3$ whether the jet is tripped or not. They may be related to differences in the nozzle geometry, as a cylindrical nozzle is used in the simulations whereas a convergent nozzle is employed in the experiments. They may also be due to other nozzle-exit conditions, such as the shear-layer thickness or the shape of the nozzle-exit profiles. Therefore, in future works, it would be relevant to investigate the influence of these conditions on the frequencies of the tones emitted by impinging jets.

References

1. Marsh AH. Noise measurements around a subsonic air jet impinging on a plane, rigid surface. *J Acoust Soc Am* 1961; 33(8): 1065–1066. DOI:10.1121/1.1908894.
2. Preisser JS. Fluctuating surface pressure and acoustic radiation for subsonic normal jet impingement. *NASA Technical Paper 1361* 1979; .

3. Neuwerth G. Acoustic feedback of a subsonic and supersonic free jet which impinges on an obstacle. *NASA Technical Translation No F-15719* 1974; .
4. Ho CM and Nosseir NS. Dynamics of an impinging jet. Part 1. the feedback phenomenon. *J Fluid Mech* 1981; 105: 119–142. DOI:10.1017/S0022112081003133.
5. Nosseir NS and Ho CM. Dynamics of an impinging jet. Part 2. the noise generation. *J Fluid Mech* 1982; 116: 379–391. DOI:10.1017/S0022112082000512.
6. Norum TD. Supersonic rectangular jet impingement noise experiments. *AIAA J* 1991; 29(7): 1051–1057. DOI:10.2514/3.10703.
7. Krothapalli A, Rajkuperan E, Alvi F et al. Flow field and noise characteristics of a supersonic impinging jet. *J Fluid Mech* 1999; 392: 155–181. DOI:10.1017/S0022112099005406.
8. Henderson B and Powell A. Experiments concerning tones produced by an axisymmetric choked jet impinging on flat plates. *J Sound Vib* 1993; 168(2): 307–326. DOI:10.1006/jsvi.1993.1375.
9. Henderson B. The connection between sound production and jet structure of the supersonic impinging jet. *J Acoust Soc Am* 2002; 111(2): 735–747. DOI:10.1121/1.1436069.
10. Henderson B, Bridges J and Wernet M. An experimental study of the oscillatory flow structure of tone-producing supersonic impinging jets. *J Fluid Mech* 2005; 542: 115–137. DOI:10.1017/S0022112005006385.
11. Dauptain A, Gicquel L and Moreau S. Large-eddy simulation of supersonic impinging jets. *AIAA J* 2012; 50(7): 1560–1574. DOI:10.2514/1.J051470.
12. Gojon R, Bogey C and Marsden O. Investigation of tone generation in ideally expanded supersonic planar impinging jets using large-eddy simulation. *J Fluid Mech* 2016; 808: 90–115. DOI:10.1017/jfm.2016.628.
13. Gojon R and Bogey C. Flow structure oscillations and tone production in underexpanded impinging round jets. *AIAA J* 2017; 55(6): 1792–1805. DOI:10.2514/1.J055618.
14. Bogey C and Gojon R. Feedback loop and upwind-propagating waves in ideally expanded supersonic impinging round jets. *J Fluid Mech* 2017; 823: 562–591. DOI:10.1017/jfm.2017.334.
15. Powell A. On edge tones and associated phenomena. *Acta Acustica United with Acustica* 1953; 3(4): 233–243.
16. Umeda Y, Maeda H and Ishii R. Hole tone generated from almost choked to highly choked jets. *AIAA J* 1988; 26(9): 1036–1043. DOI:10.2514/3.10009.
17. Umeda Y and Ishii R. Hole tone generation from highly choked jets. *J Acoust Soc Am* 1993; 94(2): 1058–1066. DOI:10.1121/1.406952.
18. Varé M and Bogey C. Generation of acoustic tones in round jets at a Mach number of 0.9 impinging on a plate with and without a hole. *J Fluid Mech* 2022; 936: A16. DOI:10.1017/jfm.2022.47.
19. Gojon R and Bogey C. Effects of the angle of impact on the aeroacoustic feedback mechanism in supersonic impinging planar jets. *International Journal of Aeroacoustics* 2019; 18(2-3): 258–278. DOI:10.1177/1475472X18812808.
20. Tam C and Ahuja K. Theoretical model of discrete tone generation by impinging jets. *J Fluid Mech* 1990; 214: 67–87. DOI:10.1017/S0022112090000052.
21. Jordan P, Jaunet V, Towne A et al. Jet-flap interaction tones. *J Fluid Mech* 2018; 853: 333–358. DOI:10.1017/jfm.2018.566.

22. Tam C and Chandramouli S. Jet-plate interaction tones relevant to over-the-wing engine mount concept. *J Sound Vib* 2020; 486: 115378. DOI:10.1016/j.jsv.2020.115378.
23. Gojon R, Bogey C and Mihaescu M. Oscillation modes in screeching jets. *AIAA J* 2018; 56(7): 2918–2924. DOI:10.2514/1.J056936.
24. Edgington-Mitchell D, Jaunet V, Jordan P et al. Upstream-travelling acoustic jet modes as a closure mechanism for screech. *J Fluid Mech* 2018; 855. DOI:10.1017/jfm.2018.642.
25. Gojon R, Gutmark E and Mihaescu M. Antisymmetric oscillation modes in rectangular screeching jets. *AIAA J* 2019; 57(8): 3422–3441. DOI:10.2514/1.J057514.
26. Mancinelli M, Jaunet V, Jordan P et al. Screech-tone prediction using upstream-travelling jet modes. *Experiments in Fluids* 2019; 60(1): 22. DOI:10.1007/s00348-018-2673-2.
27. Towne A, Cavalieri AVG, Jordan P et al. Acoustic resonance in the potential core of subsonic jets. *J Fluid Mech* 2017; 825: 1113–1152. DOI:10.1017/jfm.2017.346.
28. Schmidt OT, Towne A, Colonius T et al. Wavepackets and trapped acoustic modes in a turbulent jet: coherent structure eduction and global stability. *J Fluid Mech* 2017; 825: 1153–1181. DOI:10.1017/jfm.2017.407.
29. Bogey C. Acoustic tones in the near-nozzle region of jets: characteristics and variations between Mach numbers 0.5 and 2. *J Fluid Mech* 2021; 921. DOI:10.1017/jfm.2021.426.
30. Bogey C. Interactions between upstream-propagating guided jet waves and shear-layer instability waves near the nozzle of subsonic and nearly ideally expanded supersonic free jets with laminar boundary layers. *J Fluid Mech* 2022; 949: A41. DOI:10.1017/jfm.2022.776.
31. Wagner F. *The sound and flow field of an axially symmetric free jet upon impact on a wall*. National Aeronautics and Space Administration, 1971.
32. Jaunet V, Mancinelli M, Jordan P et al. Dynamics of round jet impingement. *AIAA Paper 2019-2769* 2019; DOI:10.2514/6.2019-2769.
33. Varé M and Bogey C. Mach number dependence of tone generation by impinging round jets. *AIAA J* 2023; : 1–15DOI:10.2514/1.J062746.
34. Zaman K. Effect of initial condition on subsonic jet noise. *AIAA J* 1985; 23(9): 1370–1373. DOI:10.2514/3.9094.
35. Bridges J and Hussain A. Roles of initial condition and vortex pairing in jet noise. *J Sound Vib* 1987; 117(2): 289–311. DOI:10.1016/0022-460X(87)90540-2.
36. Bogey C, Marsden O and Bailly C. Influence of initial turbulence level on the flow and sound fields of a subsonic jet at a diameter-based Reynolds number of 10^5. *J Fluid Mech* 2012; 701: 352–385. DOI:10.1017/jfm.2012.162.
37. Brès G, Jordan P, Jaunet V et al. Importance of the nozzle-exit boundary-layer state in subsonic turbulent jets. *J Fluid Mech* 2018; 851: 83–124. DOI:10.1017/jfm.2018.476.
38. Bogey C, Marsden O and Bailly C. Large-eddy simulation of the flow and acoustic fields of a Reynolds number 10^5 subsonic jet with tripped exit boundary layers. *Phys Fluids* 2011; 23(3): 035104. DOI:10.1063/1.3555634.
39. Varé M and Bogey C. Flow and acoustic fields of rocket jets impinging on a perforated plate. *AIAA J* 2022; : 1–14DOI:10.2514/1.J061253.
40. Varé M and Bogey C. Presence and properties of acoustic peaks near the nozzle of impinging rocket jets. *Acta Acustica* 2022; 6: 36. DOI:10.1051/aacus/2022033.
41. Berland J, Bogey C, Marsden O et al. High-order, low dispersive and low dissipative explicit schemes for multiple-scale and boundary problems. *J Comput Phys* 2007; 224(2): 637–662.

DOI:10.1016/j.jcp.2006.10.017.
42. Bogey C and Bailly C. A family of low dispersive and low dissipative explicit schemes for flow and noise computations. *J Computat Phys* 2004; 194(1): 194–214. DOI:10.1016/j.jcp.2003.09.003.
43. Fauconnier D, Bogey C and Dick E. On the performance of relaxation filtering for large-eddy simulation. *J Turbul* 2013; 14(1): 22–49. DOI:10.1080/14685248.2012.740567.
44. Bogey C, De Cacqueray N and Bailly C. A shock-capturing methodology based on adaptative spatial filtering for high-order non-linear computations. *J Comput Phys* 2009; 228(5): 1447–1465. DOI:10.1016/j.jcp.2008.10.042.
45. Tam C and Dong Z. Radiation and outflow boundary conditions for direct computation of acoustic and flow disturbances in a non uniform mean flow. *J Comput Acoust* 1996; 4(02): 175–201. DOI:10.1142/S0218396X96000040.
46. Bogey C and Bailly C. Three-dimensional non-reflective boundary conditions for acoustic simulations: far-field formulation and validation test cases. *Acta Acustica united with Acustica* 2002; 88(4): 463–471.
47. Mohseni K and Colonius T. Numerical treatment of polar coordinate singularities. *J Comput Phys* 2000; 157(2): 787–795. DOI:10.1006/jcph.1999.6382.
48. Bogey C, De Cacqueray N and Bailly C. Finite differences for coarse azimuthal discretization and for reduction of effective resolution near origin of cylindrical flow equations. *J Comput Phys* 2011; 230(4): 1134–1146. DOI:10.1016/j.jcp.2010.10.031.
49. Bogey C. Grid sensitivity of flow field and noise of high-Reynolds-number jets computed by large-eddy simulation. *International Journal of Aeroacoustics* 2018; 17(4-5): 399–424. DOI:10.1177/1475472X18778287.
50. Bogey C, Barré S and Bailly C. Direct computation of the noise generated by subsonic jets originating from a straight pipe nozzle. *International Journal of Aeroacoustics* 2008; 7(1): 1–21. DOI:10.1260/147547208784079917.
51. Viazzo S, Dejoan A and Schiestel R. Spectral features of the wall-pressure fluctuations in turbulent wall flows with and without perturbations using les. *Int J Heat Fluid Flow* 2001; 22(1): 39–52. DOI:10.1016/S0142-727X(00)00074-6.
52. Schlatter P, Li Q, Brethouwer G et al. Simulations of spatially evolving turbulent boundary layers up to $Re_\theta = 4300$. *Int J Heat Fluid Flow* 2010; 31(3): 251–261. DOI:10.1016/j.ijheatfluidflow.2009.12.011.
53. Gloerfelt X and Berland J. Turbulent boundary-layer noise: direct radiation at Mach number 0.5. *J Fluid Mech* 2013; 723: 318–351. DOI:10.1017/jfm.2013.134.
54. Kremer F and Bogey C. Large-eddy simulation of turbulent channel flow using relaxation filtering: Resolution requirement and Reynolds number effects. *Computers & Fluids* 2015; 116: 17–28. DOI:10.1016/j.compfluid.2015.03.026.
55. Michalke A. Survey on jet instability theory. *Progress in Aerospace Sciences* 1984; 21: 159–199. DOI:10.1016/0376-0421(84)90005-8.
56. Bogey C and Sabatini R. Effects of nozzle-exit boundary-layer profile on the initial shear-layer instability, flow field and noise of subsonic jets. *J Fluid Mech* 2019; 876: 288–325. DOI:10.1017/jfm.2019.546.
57. Bogey C. Generation of excess noise by jets with highly disturbed laminar boundary-layer profiles. *AIAA J* 2021; 59(2): 569–579. DOI:10.2514/1.J059610.

58. Morris P. The instability of high speed jets. *International Journal of Aeroacoustics* 2010; 9(1-2): 1–50. DOI:10.1260/1475-472X.9.1-2.1.
59. Karami S, Edgington-Mitchell D, Theofilis V et al. Characteristics of acoustic and hydrodynamic waves in under-expanded supersonic impinging jets. *J Fluid Mech* 2020; 905. DOI:10.1017/jfm.2020.740.
60. Woolley J and Karamcheti K. The role of jet stability in edgetone generation. *AIAA Paper* 1973; (73-628): 1–35. DOI:10.2514/6.1973-628.
61. Woolley J and Karamcheti K. Role of jet stability in edgetone generation. *AIAA J* 1974; 12(11): 1457–1458. DOI:10.2514/3.49525.
62. Tam C, Chen P and Seiner J. Relationship between the instability waves and noise of high-speed jets. *AIAA J* 1992; 30(7): 1747–1752. DOI:10.2514/3.11132.
63. Muller F, Vuillot F, Rahier G et al. Modal analysis of a subsonic hot jet les with comparison to the linear stability analysis. *AIAA Paper* 2005; : 2886DOI:10.2514/6.2005-2886.